Geophysical Research Letters

Supporting Information for

Acoustics reveals short-term air temperature fluctuations near Mars' surface

Baptiste Chide[1], Tanguy Bertrand[2], Ralph D. Lorenz[3], Asier Munguira[4], Ricardo Hueso[4], Agustin Sánchez-Lavega[4], German Martinez[5, 6], Aymeric Spiga[7,8], Xavier Jacob[9], Manuel de la Torre Juarez[10], Mark Lemmon[11], Don Banfield[12], Claire E. Newman[13], Naomi Murdoch[14], Alexander Stott[14], Daniel Viúdez-Moreiras[15], Jorge Pla-Garcia[15], Carène Larmat[1], Nina L. Lanza[1], José Antonio Rodríguez-Manfredi[15], Roger C. Wiens[16]

[1]: Space and Planetary Exploration Team, Los Alamos National Laboratory, Los Alamos, New Mexico, USA. [2]: LESIA, Observatoire de Paris, Université PSL, Sorbonne Université, Université de Paris, CNRS, Meudon, France. [3]: Space Exploration Sector, Johns Hopkins Applied Physics Laboratory, Laurel, MD, USA. [4]. Física Aplicada, Escuela de Ingeniería de Bilbao, UPV/EHU, Bilbao, Spain. [5]: Lunar and Planetary Institute, Universities Space Research Association, Houston, TX, USA. [6]: Department of Climate and Space Sciences and Engineering, University of Michigan, Ann Arbor, MI, USA. [7]: Laboratoire de Météorologie Dynamique, Institut Pierre-Simon Laplace (LMD/IPSL), Sorbonne Université, Centre National de la Recherche Scientifique (CNRS), École Polytechnique, École Normale Supérieure (ENS), Paris, France. [8] : Institut Universitaire de France, Paris, France. [9] : Institut de Mécanique des Fluides de Touloue, Université de Toulouse III Paul Sabatier, INP, CNRS, Toulouse, France. [10] : Jet Propulsion Laboratory, California Institute of Technology, Pasadena, California, USA. [11]: Space Science Institute, Boulder, CO 80301, USA. [12] : NASA Ames Research Center, Mountain View, CA, USA. [13] : Aeolis Research, Chandler, AZ, USA. [14]: Institut Supérieur de l'Aéronautique et de l'Espace (ISAE-SUPAERO), Université de Toulouse, Toulouse, France. [15]: Centro de Astrobiología (INTA-CSIC), Madrid, Spain. [16]: Department of Earth, Atmospheric, and Planetary Sciences, Purdue University, West Lafayette, IN, USA

Contents of this file

Introduction

Text S1 to Text S3 and Figure S1 describe the observations, datasets and models. Text S4 to Text S6 give the details of the methods, the processing and the equations used to measure the sound speed and compute the associated sonic temperature and its fluctuations. Finally, Text S7 and Figures S2 and S3 illustrate the dispersion of the temperature fluctuation observed with the microphone and detail the method to assess the potential thermal contamination from the radioisotope thermal generator of Perseverance

Text S1. SuperCam observations

The SuperCam instrument suite (Wiens et al., 2020; Maurice et al., 2021) combines four analytical techniques to study at remote distances the chemistry and mineralogy of Mars' surface, and the local environment. Added to them, it includes a microphone, which was primarily designed to complement the Laser-Induced Breakdown Spectroscopy (LIBS) investigation (Chide et al., 2020, 2021, Murdoch et al., 2019). From the top of the rover mast, it records the acoustic signal generated by the shock wave that results from the expansion of the hot laser-induced plasma in Mars rarified atmosphere. A LIBS typical analysis of a target consists of several separate bursts of 30 to 150 pulsed-laser shots (Maurice et al., 2021), which are fired at a cadence of 3 Hz (total duration of a burst of shots is between 10 s and 50 s). For each target, 5 to 10 bursts are repeated on points separated by a few millimeters to assess the heterogeneity of the target itself. Altogether, a LIBS analysis of a Mars' surface targets lasts about 20 min. Each laser-induced acoustic wave is recorded over a 60 ms time-window triggered 743 µs before laser ignition. As the laser-induced shock waves are well localized in time and space, the propagation time of the sound wave yields to the speed of sound. The N-wave that is created by LIBS is very short and exhibits an acoustic signature above 2 kHz (Maurice et al., 2022). For each time series, frequencies below 2 kHz are filtered out to remove the contribution that are not explicitly related to the shock wave itself. Hence, the speed of sound is calculated each time the laser is fired. The data set under consideration includes acoustic time series from 188 targets located at distances from 2.05 m to 6 m from the rover (targets recorded further are excluded from the data set because of a poor signal-to-noise ratio). For operational reasons, LIBS targets have been acquired during the daytime, mostly between 11:00 and 14:00 Local True Solar Time (LTST), with a few ones acquired early morning (the earliest target is at 8:49 LTST) or late afternoon (the latest is at 18:40 LTST). The ~15:00 LTST timeframe, where there is a gap in SuperCam measurements, is mostly dedicated to rover operations such as driving. They are randomly distributed over the mission duration (from target Hedgehog on Sol 37, L_s=24°, to Alfalfa on Sol 378, L_s=190°).

Text S2. MEDA atmospheric survey

MEDA is a multi-sensor weather station that includes 2 Wind Sensors (WS), 5 Air Temperature Sensors (ATS) and several thermopiles sensitive to infrared radiation in the Thermal InfraRed Sensor (TIRS), the first in-situ Martian IR radiometer. Additional meteorological variables are also measured by MEDA (Rodriguez-Manfredi et al., 2021). The WS and ATS operate up to 2 Hz, whereas TIRS and all other MEDA sensors record data at 1 Hz. The wind measurements are obtained by two booms on the Remote Sensing Mast (RSM) located 120 degrees of azimuth apart from each other to ensure that accurate winds can be obtained in most orientations. The 5 ATS are located at two altitudes: two in front of the rover and the three others on the RSM. The latter are at 1.45 m above the ground and are distributed azimuthally so that at least one sensor is always in upwind conditions. The former are at 0.84 m above the ground, and are partially sheltered from the environment winds by the rover itself. All record very small thermal fluctuations except when winds are directed towards the sensors. Indeed, in general MEDA measures the temperatures of different eddies that are being carried by the local wind to the ATS. For slow winds and/or an unfavorable orientation, MEDA temperature sensors might be shielded from their environment. This observational bias is even more pronounced for MEDA temperature sensors at the rover's deck height, because the temperature estimation is based on two sensors that are closer to warm equipment of the rover.

TIRS measures the air temperature with peak emission at about 40 m, and the surface brightness temperature (Martínez et al., this issue). The field of view of the ground temperature channel covers an ellipsoid area of 3–4 m^2, whose center is ~3.75 m away from Perseverance Radioisotope Thermoelectric Generator (RTG) to minimize thermal contamination. MEDA data are acquired through 1-hour long sessions that alternate between even and odd hours each sol (duty cycle = 50%). Hence, MEDA generally performs a complete diurnal cycle from the combination of two consecutive Sols. Wind data are obtained more intermittently due to operational constraints (e.g. WS must be off during communication passes). Additional gaps in the data can appear as a consequence of power and data volume restrictions in particular Sols.

For each SuperCam observation, when MEDA wind (speed and direction) and air temperature exist, MEDA data are interpolated to the time of SuperCam observations to allow a direct comparison at short timescales. For seasonal and diurnal studies, MEDA data are averaged over 10 min, for every daytime hour and every Sol in order to extract a seasonal and diurnal evolution with as few discontinuities as possible. This stands in contrast to the sampling frequency of SuperCam, which is non-uniform over a day and over the mission.

To provide geophysical context across Perseverance's traverse, we use values of thermal inertia and sensible heat flux determined by MEDA, following methods discussed in Martínez et al., (this issue). In addition, we use the covariance between vertical wind and air temperature, also called *w'T'*, which is derived for the first time on Mars from MEDA measurements by dividing the sensible heat flux by the air density and the specific heat of CO_2, 738 J/kg/K. The sensible heat flux is derived by requiring surface energy balance, which is made possible because MEDA measures all radiative contributions (see more details in Martínez et al., (this issue)). Finally, we refer occasionally to optical depth values, which are retrieved from the MastCam-Z instrument (Bell et al., 2021).

Text S3. Climate models (MCD and LES)

The Mars Climate Database (MCD) predictions are derived from global 3D simulations of Mars' atmosphere performed with the Mars Global Climate Model (GCM), developed at the Laboratoire de Météorologie Dynamique, Paris, France (Forget et al., 1999). We used the MCD Version 5.3 (Millour et al., 2018) and we have extracted results from two scenarii: (1) The "climatology scenario", in which the simulated spatial and vertical dust distribution is reconstructed from observations over Martian Years 24 to 31 without global dust storms (thus representative of standard climate conditions), and in which average solar EUV conditions are assumed. (2) The "warm scenario", which corresponds to "dusty conditions" (the dust opacity at a given location is set to the maximum observed, unless during a global dust storm in which case it is further increased by 50%), topped with a solar maximum thermosphere. Here, MCD outputs are compared with air temperature values (see Section 3.1)

Large-Eddy Simulations (LES) have a spatial resolution of several tens of meters. Hence, the model resolves the largest turbulent eddies in the daytime Martian PBL, which are responsible for most of the transport of heat and momentum there, including the convective cells, gusts, and vortices (Michaels & Rafkin, 2004; Spiga et al., 2010; Toigo et al., 2003). However, the very-small-scale "local" eddies and turbulence, such as probed by the microphone, are still not resolved by LES. Although this strongly limits the use of LES to interpret our observations, qualitative and quantitative comparisons of interest can still be made, especially given that the LES technique captures the signatures of convective cells and vortices. Here we use the model described in Spiga and Forget (2009) and Spiga et al., (2010) which couples the Weather Research and Forecast hydrodynamical solver (Skamarock & Klemp, 2008), and run at high spatial and temporal resolutions that are typical of LES (Moeng et al., 2007), to the physical parameterizations, notably radiative transfer, developed for Mars at the Laboratoire de Météorologie Dynamique (LMD; see Forget et al., 1999; Madeleine et al., 2011).

LES simulations are performed following the idealized setting of an infinite flat plain through doubly periodic boundary conditions. We used the same settings as those described in Spiga et al., (2021) for a study of InSight observations, with the exception that we have adapted the simulations to: (1) the location and surface condition of Jezero crater, with a thermal inertia of 350 J m^{-2} K^{-1} $s^{-1/2}$ and an albedo of 0.15, in good agreement with orbital and in situ observations (e.g., Martínez et al., this issue), and (2) the atmospheric environment at Ls=60°, with an ambient wind speed of 10 $m.s^{-1}$ and a visible column dust opacity of 0.32, based on MCD predictions. The spatial resolution is 25 m (with an integration time step of 1/4 s), for a total extent of the simulation domain of 12 km. The top of the model is set at 10 km altitude with 241 vertical levels. More details regarding the model settings and initialization are given in Spiga et al., (2021).

The smallest eddies resolved by the LES are roughly larger than about three times the spatial resolution. Therefore, only eddies larger than 75 m are resolved by the LES performed here, corresponding to a typical timescale of 30 s. In order to simulate eddies developing over a timescale of 0.2 s, the model should use a resolution of 0.16 m, which is not achievable by LES models. Instead, Direct Numerical Simulations (DNS) should be used (Bury et al., 2019).

Text S4. Sound speed measurements

The arrival time of the acoustic wave is determined when the compression wave arrives and its amplitude reaches 2% of the maximum peak amplitude. Considering the 100 kHz sampling rate of the microphone, there is an uncertainty of 10 µs for each laser shot, i.e. ±0.05% for a propagation time of 10 ms. SuperCam targets are located at a median distance of 2.6 m where the median propagation time is 10 ms. The distance from the target to the microphone is retrieved within ±0.33 % for targets at 7m owing to the autofocus capability of the SuperCam telescope (Maurice et al. 2021). However, an autofocus is only performed on the first and last points of a 5 or 10 bursts raster, and occasionally at one or two intermediate points. The targets can have voids, highs, lows, or a gradual rock topography that slightly modify the point-to-instrument distance compared to the distance retrieved on the closest autofocus point. Considering all the targets analyzed so far, the distance variation between two successive autofocuses is 0.5% of the total distance, which dominates the uncertainty on the point-to-target distance. This error is constant for all shots in a given burst. Given the error budget on the distance and the propagation time, the total uncertainty of the retrieved sound speed is ±0.55 %. During the early stage of the laser-induced plasma expansion, the pressure front propagates at supersonic speed, namely a shock wave, before it weakens to an acoustic wave traveling at sonic speed (Zel'dovich & Raizer, 1967). Under Mars atmosphere conditions, the shock wave is observed to reach sonic speed after 23 µs and a distance of 15 mm (*i.e.* an average speed of 652 m/s) (Seel, 2021). Therefore, the sound speed is computed only over the sonic part of the propagation path.

Given the strong vertical temperature gradient in the atmosphere during the daytime, the sound speed decreases along the acoustic propagation path. The gradient of temperature T as a function of the height z can be modeled with a "bulk" approximation using a log-profile in the surface layer:

$$T(z) = T_0(z/z_0)^{-b} \quad (1)$$

with z_0 =1 cm chosen as the roughness length (the model intercomparison study of Newman et al., (2021), showed a range from 7.4 mm to 3cm, depending on the orbitally-derived dataset used), and T_0 the temperature associated with this height.

The sound speed measured in this study, c_{mes}, can be written as a function of the distance D and the propagation path t_{path}:

$$c_{mes} = \frac{D}{t_{path}} \quad (2)$$

Considering the propagation time as the sum of all the elemental propagation time over the acoustic path. Then the propagation time can be written as follow:

$$t_{path} = \int_0^H \frac{D}{Hc(z)} dz \quad (3)$$

Or considering an ideal gas law, the sound speed $c(z)$, at the altitude z can be written as:

$$c(z) = \sqrt{\frac{\gamma RT(z)}{M}} \quad (4)$$

with M being the molecular mass of the atmosphere, $T(z)$ the temperature at the height z, R the ideal gas constant and γ the specific heat ratio. Substituting (1) and (4) into (2) it comes:

$$t_{path} = \frac{D}{H}\int_0^H \sqrt{\frac{\gamma RT(z)}{M}} dz$$

$$t_{path} = \frac{D}{H}\sqrt{\frac{M}{\gamma R\, T_0}}\int_0^H \left(\frac{z}{z_0}\right)^{\frac{b}{2}} dz$$

$$t_{path} = \frac{D}{H}\sqrt{\frac{M}{\gamma R\, T_0}}\frac{1}{z_0^{\frac{b}{2}}}\left[\frac{z^{\frac{b}{2}+1}}{\frac{b}{2}+1}\right]_0^H$$

$$t_{path} = \frac{D\sqrt{\frac{M}{\gamma R\, T_0}}\left(\frac{H}{z_0}\right)^{\frac{b}{2}}}{\frac{b}{2}+1} \quad (5)$$

Then the measured sound speed writes:

$$c_{mes} = \frac{\frac{b}{2} + 1}{\sqrt{\frac{M}{\gamma R\, T_0}} \left(\frac{H}{z_0}\right)^{\frac{b}{2}}}$$

$$c_{mes} = \sqrt{\frac{\gamma R\, T_0}{M} \left(\frac{z_0}{H}\right)^{b} \left(\frac{b}{2} + 1\right)^{2}} \quad (6)$$

Therefore, the associated sonic temperature T_{mes} writes:

$$T_{mes} = T_0 \left(\frac{z_0}{H}\right)^{b} \left(\frac{b}{2} + 1\right)^{2} \qquad (7)$$

By identifying it with Equation (1), it comes that the equivalent height z_{eq} can be expressed as follow:

$$T_0 \left(\frac{z_{eq}}{z_0}\right)^{b} = T_0 \left(\frac{z_0}{H}\right)^{b} \left(\frac{b}{2} + 1\right)^{2}$$

$$z_{eq} = H * \left(1\ + \frac{b}{2}\right)^{-\frac{2}{b}} \qquad (8)$$

It turns that the sound speed measured with the microphone is equivalent to the sound speed at 0.77 m above the ground. As shown in Equation (8), this value is independent from the rover-to-target distance.

Similar to optical mirages, the temperature decrease with height is also responsible for a refraction upward of the acoustic beam across layers of different temperatures. Considering the same thermal gradient as before, the curved propagation path is less than 0.01 % longer than the non-refracted beam for a target located at 6 m, *i.e.* the farthest distance considered here. Thus, this mirage effect can be neglected.

Text S5. Sonic temperature computation

The sonic temperature is obtained using the ideal gas law (see Equation (4) in Text S4). γ the specific heat ratio can be written as:

$$\gamma = \frac{C_V + R}{C_V} \qquad (9)$$

with C_v the isochoric specific heat. However, due to the unique properties of the carbon dioxide molecules at low pressure, for acoustic waves with a frequency higher than ~240 Hz (i.e. the relaxation frequency of CO_2 at a pressure of ~6 mbar), CO_2 vibrational modes activated through collisions do not have time to relax their energy to translational modes (Zhang et al., 2020). Laser-induced acoustic waves have a frequency content higher than 2 kHz and therefore belong to this unrelaxed regime where the isochoric specific heat needs to be corrected from the vibrational contribution. Hence, the high-frequency isochoric specific heat $C_{v,\infty}$ is determined as (Bass and Chambers, 2001):

$$\frac{C_{V,\infty}}{R} = \frac{C_{V,0}}{R} - \frac{\left[2 * 0.95 * \left(\frac{960}{T}\right)^2 * e^{-\frac{960}{T}}\right]}{\left[1 - e^{-\frac{960}{T}}\right]^2}$$

with $C_{v,0}$, being the low frequency specific heat and the second term representing the contribution of the molecule vibration to the specific heat, considering that most of it comes from the double degenerate bending mode (v2) whose vibrational temperature is 960 K. Thermodynamics parameters, M and $C_{v,0}$, that are used to compute $C_{v,\infty}$ and subsequently γ are extracted from the Mars Climate Database. Evolutions of M and γ over the time period considered in this study are represented in Supporting Fig. S1.

The relative uncertainty of ±0.55% on the sound speed translates into a relative uncertainty of ±1.1 % on the associated sonic temperature. It corresponds to an absolute uncertainty of 3.8 K for a measured sonic temperature of 250 K (average temperature at 13:00 LTST) and an absolute uncertainty of 2.5 K for 230 K (average temperature at 9:00 and 18:00 LTST).

Text S6. Temperature fluctuation retrieval

For each laser burst, ranging from 30 to 150 consecutive shots over 10 to 50 s, the temperature derivative is computed as the gradient over this time series (second order accurate central differences in the interior points). Then, the temperature fluctuation is computed as the full width at half maximum of the distribution of the temperature derivative (see histogram in Fig. 3e). Each histogram is made with 150 points. For bursts of 150 shots, one histogram is built per burst. For bursts of 30 shots, the histogram is made by concatenating the temperature derivatives from 5 successive bursts, i.e. one raster of five points or half a raster of 10 points. For MEDA data (see blue histograms in Fig. 3e), when available in parallel with microphone data, the fluctuations are computed exactly the same way.

Text S7. Distribution of the difference between sonic and MEDA temperatures

The distribution of the difference between sonic temperatures and MEDA temperatures are represented in Supporting Information Fig. S2. It shows that the fitted Gaussian distribution is centered around 0.6 K, which means that the sonic temperatures are statistically 0.6 K higher than MEDA temperatures at 0.84 m. This is consistent with a decreasing temperature with height, as the equivalent height for sonic temperatures is 0.77 m. If we refer to the evolution of the temperature given in Equation (1), the temperature at 0.77 m should be 0.4 K higher than the temperature at 0.84 m which is consistent with the order of magnitude found here.

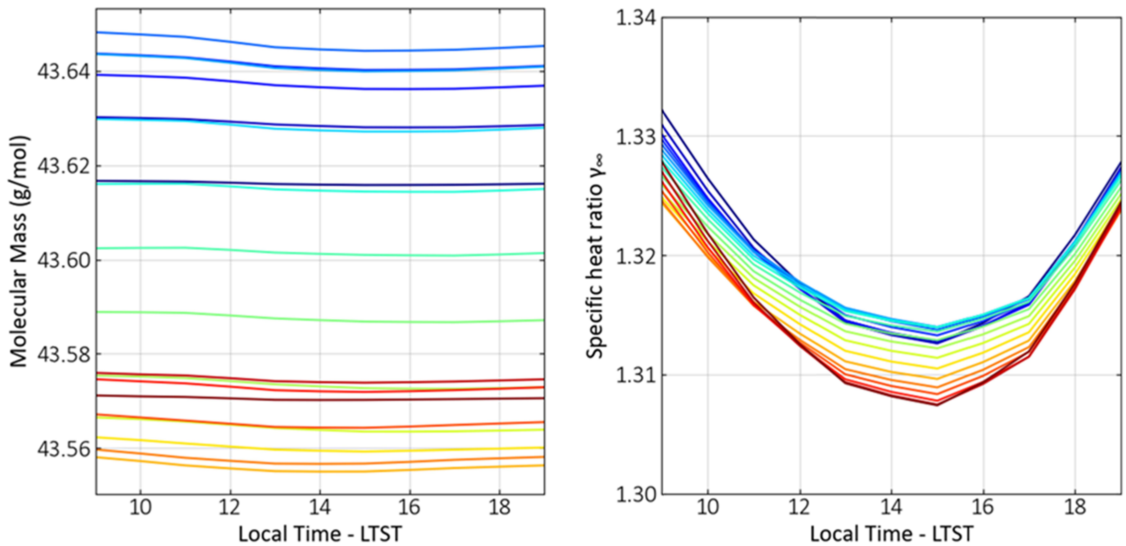

Figure S1. Daytime evolution of the thermodynamic parameters extracted from the Mars Climate Database at Jezero crater coordinate and used for the computation of the acoustic temperature. (a) molecular mass, (b) adiabatic ratio at high frequency. The color code indicates the solar longitude, from darkblue (Ls=0°) to darkred (Ls=190°).

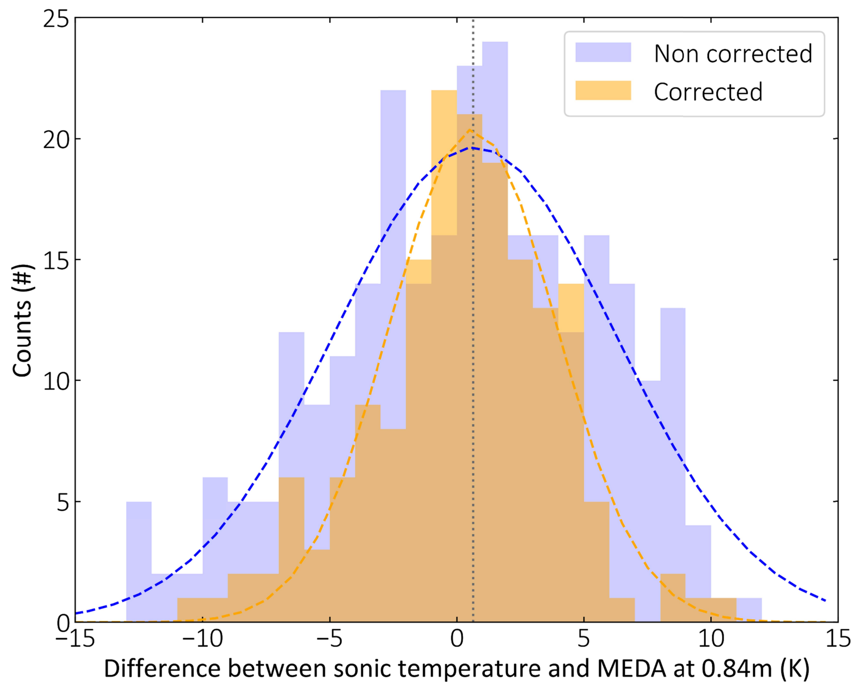

Figure S2. Distribution of the difference between the sonic temperature (non-corrected in blue, corrected form the wind in orange) and MEDA temperature at 0.84 m for all the points considered in this study. They are fitted with a Gaussian function (dashed lines). The vertical dotted line represents the center of the Gaussian for the corrected points, 0.6 K.

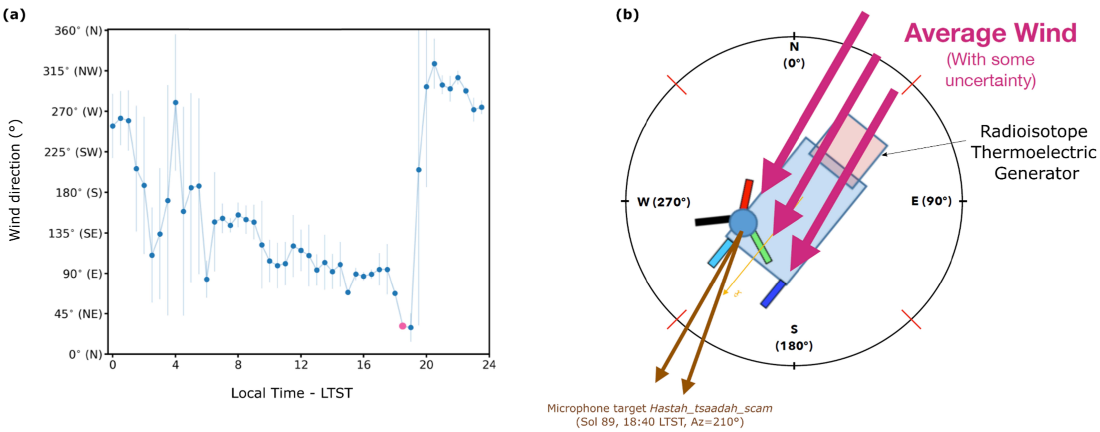

Figure S3. Thermal contamination from the RTG that could explain the large temperature fluctuation event observed at 18:40 on Sol 89. (a) Mean wind direction averaged over 20 Sols around the event (Sols 86 to 105). The pink dot indicates a mean wind direction of 30° at 18:40 LTST. (b) Geometry of the acoustic path for this observation with regard to the rover orientation (SW) and wind direction. Munguira et al., (this issue) has shown that this effect is typically observed at night, and happens only for a very specific rover heading with regard to the wind. Moreover, the higher temperatures and stronger winds during the daytime are more likely to mask this effect. Therefore, it is considered that this effect has almost no impact on the results presented in this study.

References

From the special issue:

Martínez G. et al. (2022) Thermal Inertia, Albedo and Surface Energy Budget at Jezero Crater, Mars, as observed from the Mars 2020 MEDA instrument. *Journal of Geophysical Research: Planets*, this issue.

Bass, H. E., & Chambers, J. P. (2001). Absorption of sound in the Martian atmosphere. The Journal of the Acoustical Society of America, 109(6), 3069-3071. doi: 10.1121/1.1365424

Bell, J.F., Maki, J.N., Mehall, G.L., Ravine, M.e., Caplinger, M.A., … Wolff, M.J. (2021). The Mars 2020 Perseverance Rover Mast Camera Zoom (Mastcam-Z) Multispectral, Stereoscopic Imaging Investigation. Space Science Reviws 217, 24. https://doi.org/10.1007/s11214-020-00755-x

Bury, Y., Chide, B., Murdoch, N., Cadu, A., Mimoun, D., & Maurice, S. (2019). Wake-induced pressure fluctuations on the Mars2020/SuperCam microphone inform on Martian wind properties. In EPSC-DPS Joint Meeting.

Chide, B., Beyssac, O., Gauthier, M., Benzerara, K., Estève, I., Boulliard, J.-C., … Wiens, R. C. (2021). Acoustic monitoring of laser-induced phase transitions in minerals: implication for mars exploration with SuperCam. Scientific Reports, 11(1). doi: 10.1038/s41598-021-03315-7

Chide, B., Maurice, S., Cousin, A., Bousquet, B., Mimoun, D., Beyssac, O., … Wiens, R. C. (2020). Recording laser-induced sparks on mars with the SuperCam microphone. Spectrochimica Acta Part B: Atomic Spectroscopy, 174, 106000. doi: 10.1016/j.sab.2020.106000

Forget, F., Hourdin, F., Fournier, R., Hourdin, C., Talagrand, O., Collins, M., … Huot, J.-P. (1999). Improved general circulation models of the martian atmosphere from the surface to above 80 km. Journal of Geophysical Research: Planets, 104(E10), 24155-24175. doi: 10.1029/1999je001025

Madeleine, J.-B., Forget, F., Millour, E., Montabone, L., & Wolff, M. J. (2011). Revisiting the radiative impact of dust on mars using the LMD global climate model. Journal of Geophysical Research, 116(E11). doi: 10.1029/2011je003855

Maurice, S., Wiens, R. C., Bernardi, P., Caïs, P., Robinson, S., Nelson, T., … Wong, K. W. (2021). The SuperCam instrument suite on the mars 2020 rover: Science objectives and mast-unit description. Space Science Reviews, 217(3). doi: 10.1007/s11214-021-00807-w

Michaels, T. I., & Rafkin, S. C. R. (2004). Large-eddy simulation of atmospheric convection on mars. Quarterly Journal of the Royal Meteorological Society, 130(599), 1251-1274. doi: 10.1256/qj.02.169

Millour, E., Forget, F., Spiga, A., Vals, M., Zakharov, V., Montabone, L., … Cipriani, F. (2018). The Mars Climate Database Version 5.3. In Scienti_c Workshop: From Mars Express to ExoMars. ESAC Madrid, Spain.

Moeng, C.-H., Dudhia, J., Klemp, J., & Sullivan, P. (2007). Examining two-way grid nesting for large eddy simulation of the PBL using the WRF model. Monthly Weather Review, 135(6), 2295-2311. doi: 10.1175/mwr3406.1

Murdoch, N., Chide, B., Lasue, J., Cadu, A., Sournac, A., Bassas-Port_us, M., … Mimoun, D. (2019). Laser-induced breakdown spectroscopy acoustic testing of the mars 2020 microphone. Planetary and Space Science, 165, 260- 271. doi: 10.1016/j.pss.2018.09.009

Newman, C. E., de la Torre Juarez, M., Pla-Garcia, J., Wilson, R. J., Lewis, S. R., Neary, L., … Rodriguez-Manfredi, J. A. (2021). Multi-model meteorological and aeolian predictions for mars 2020 and the jezero crater region. Space Science Reviews, 217(1). doi: 10.1007/s11214-020-00788-2

Rodriguez-Manfredi, J. A., de la Torre Juarez, M., Alonso, A., Apestigue, V., Arruego, I., Atienza, T., … Zurita, S. (2021). The mars environmental dynamics analyzer, MEDA. a suite of environmental sensors for the mars 2020 mission. Space Science Reviews, 217(3). doi: 10.1007/s11214-021-00816-9

Seel, F. (2021). Laboratory studies on laser-induced shock waves for libs measurements on mars (Master's thesis, Technische Universitat Berlin). Retrieved from https://elib.dlr.de/145314/

Skamarock, W. C., & Klemp, J. B. (2008). A time-split nonhydrostatic atmospheric model for weather research and forecasting applications. Journal of Computational Physics, 227(7), 3465-3485. doi: 10.1016/j.jcp.2007.01.037

Spiga, A., & Forget, F. (2009). A new model to simulate the martian mesoscale and microscale atmospheric circulation: Validation and first results. Journal of Geophysical Research, 114(E2). doi: 10.1029/2008je003242

Spiga, A., Forget, F., Lewis, S. R., & Hinson, D. P. (2010). Structure and dynamics of the convective boundary layer on mars as inferred from large-eddy simulations and remote-sensing measurements. Quarterly Journal of the Royal Meteorological Society, 136(647), 414-428. doi: 10.1002/qj.563

Spiga, A., Murdoch, N., Lorenz, R., Forget, F., Newman, C., Rodriguez, S., … Banerdt, W. B. (2021). A study of daytime convective vortices and turbulence in the martian planetary boundary layer based on half-a-year of InSight atmospheric measurements and large-eddy simulations. Journal of Geophysical Research: Planets, 126(1). doi: 10.1029/2020je006511

Toigo, A. D., Richardson, M. I., Ewald, S. P., & Gierasch, P. J. (2003). Numerical simulation of martian dust devils. Journal of Geophysical Research, 108(E6). doi: 10 .1029/2002je002002

Wiens, R. C., Maurice, S., Robinson, S. H., Nelson, A. E., Cais, P., Bernardi, P., … Willis, P. (2020). The SuperCam instrument suite on the NASA mars 2020 rover: Body unit and combined system tests. Space Science Reviews, 217(1). doi: 10.1007/s11214-020-00777-5

Zel'dovich, Y., & Raizer, Y. (1967). Physics of shock waves and high-temperature hydrodynamic phenomena. Elsevier. doi: 10.1016/b978-0-12-395672-9.x5001-2

Zhang, X., Wang, S., & Zhu, M. (2020). Locating the inflection point of frequency-dependent velocity dispersion by acoustic relaxation to identify gas mixtures. Measurement Science and Technology, 31(11), 115001. doi: 10.1088/1361-6501/ab9375